Polymer Journal
https://doi.org/10.1038/s41428-024-00917-6

ORIGINAL ARTICLE

Changes in crystal morphology induced by lanthanide doping into diacetylene lamellar crystals

Michinari Kohri[1] · Sojiro Isomura[1] · Kyoka Tachibana[1] · Ryota Hikichi[2] · Yuya Oaki[2] · Hiroki Wadati[3,4] · Hirofumi Kanoh[5] · Keiki Kishikawa[1]

Received: 4 March 2024 / Revised: 19 April 2024 / Accepted: 20 April 2024

Abstract

In this study, we show that doping lanthanides into lamellar crystals reorganizes the lamellar structure and dramatically changes the crystal morphology. **Azo-DA**, a compound with azobenzene derivatives and carboxylic acids at both ends of the diacetylene moiety, formed plate-like lamellar crystals. The doping of holmium (Ho), a lanthanide, into the film obtained by stacking **Azo-DA** lamellar crystals, promoted a dramatic change in crystal morphology, resulting in the formation of an **Azo-DA/Ho** film with a radial lamellar crystal structure. A detailed investigation of the crystal growth process revealed that **Azo-DA/Ho**, which is slightly formed in the solution phase during Ho doping, acts as a pseudonucleating agent and dramatically changes the morphology of the lamellar crystals. Additionally, the morphological changes in the lamellar crystal films significantly changed the surface properties of the films, such as their appearance and water repellency. Similar morphological changes in lamellar crystals were induced when other lanthanide elements were used instead of Ho, and the type of lanthanide dopant can affect the magnetic properties of the films.

Introduction

In general, crystalline linear polymers assume a lamellar structure [1–4]. The kinetically dominant lamellar thickness (longitudinal spread) is considerably shorter than the fully extended chain length of the polymer, often by a few nanometers [5, 6]. On the other hand, lamellar crystals often extend a few microns in width [7, 8]. Lamellar crystal morphologies result from nucleation and kinetics in the early stages of crystal growth [9–11]. To artificially alter the morphology of lamellar crystals, approaches for controlling crystal nucleation in the early stages have been reported. For example, homoepitaxial crystallization of poly(ε-caprolactone) on a substrate surface with controlled orientation topology results in a structure of edge-on lamellae arranged parallel to the substrate [12]. The improved crystallization of secondary polymers from the nanofiber surface results kebab lamellar layer and shish-kebab-type hierarchical crystal structure formation. In these systems, the substrate and nanofibers act as 1D nucleators, and their surface properties lead to unique morphological changes in crystal shape [13].

Polydiacetylene (PDA), a conjugated polymer, has unique colorimetric transition properties in response to various external stimuli and has been investigated for numerous applications as a biosensor and chemosensor over the past several decades [14–17]. Diacetylene (DA) monomers often self-assemble into regular lamellar structures over long distances. The flexibility of DA monomer design allows for controlling its self-assembling behavior and creating lamellar structures with various morphologies, such

Supplementary information The online version contains supplementary material available at https://doi.org/10.1038/s41428-024-00917-6.

✉ Michinari Kohri
kohri@faculty.chiba-u.jp

[1] Department of Applied Chemistry and Biotechnology, Graduate School of Engineering, Chiba University, 1-33 Yayoi-cho, Inage-ku, Chiba 263-8522, Japan

[2] Department of Applied Chemistry, Faculty of Science and Technology, Keio University, 3-14-1 Hiyoshi, Kohoku-ku, Yokohama 223-8522, Japan

[3] Department of Material Science, Graduate School of Science, University of Hyogo, Ako, Hyogo 678-1297, Japan

[4] Institute of Laser Engineering, Osaka University, Suita, Osaka 565-0871, Japan

[5] Department of Chemistry, Graduate School of Science, Chiba University, 1-33 Yayoi-cho, Inage-ku, Chiba 263-8522, Japan

Published online: 15 May 2024

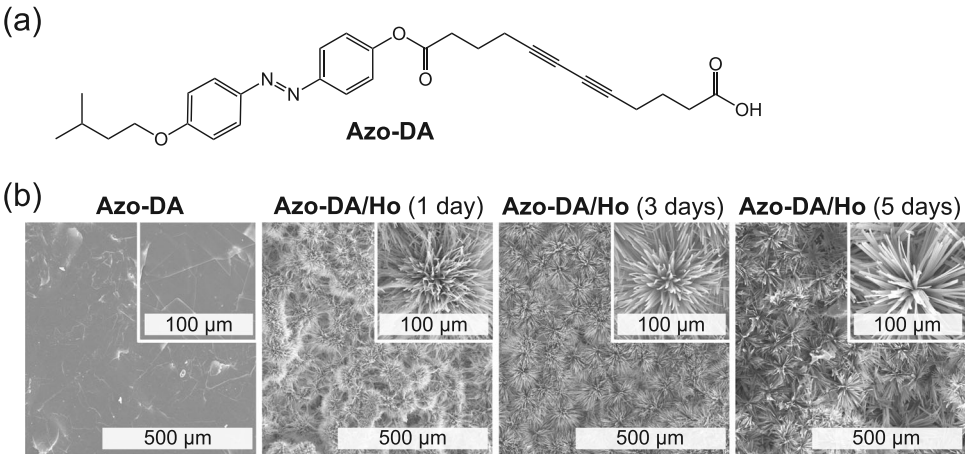

Fig. 1 **a** Chemical structure of **Azo-DA**. **b** SEM images of the surfaces of the **Azo-DA** and **Azo-DA/Ho** films immersed in Ho solution for 1, 3, and 5 days

as vesicles, films, fibers, plates, and particles [18–20]. We recently reported that lamellar structures of compounds with azobenzene moieties introduced at both ends of the DA unit form plate-like crystals; the resulting films of stacked plate-like crystals exhibited gold-like metallic lusters [21]. In DA-based self-assembly, intermolecular interactions such as hydrogen bonding, π-π stacking, van der Waals interactions, hydrophobic interactions, and metal-ligand coordination are the driving forces of organization [22–24]. Most of the literature on PDA focuses on providing chromism properties to PDA, which is caused by distortion of the PDA main chain [25–27]. A few papers mention crystal rearrangements induced by external stimuli to DA lamellar crystals. For example, Takajyo et al. reported the topochemical polymerization of DA induced by electric pulse injection into DA lamellar crystals through a scanning tunneling microscope tip [28]. Kim et al. showed that the mechanical pressure (2–150 MPa) applied to DA lamellar crystals induces a crystalline phase transition and controls topochemical polymerization behavior [29]. The fact that the electrical and mechanical stimulation of DA lamellar crystals induces crystalline phase transitions motivated us to further investigate other external stimulus adaptations that are simpler and do not require equipment.

Here, we show the reorganization of lamellar crystals and the dramatic change in crystal morphology induced by doping lanthanides into DA lamellar crystals. **Azo-DA**, centered on the DA moiety with an azobenzene derivative on one side chain and a carboxylic acid, which acts as a chelating site for lanthanide, formed plate-like lamellar crystals by a simple recrystallization process (Fig. 1a, b). Doping holmium (Ho) [30, 31], a lanthanide, into the film obtained by stacking **Azo-DA** plate-like lamellar crystals dramatically changed the crystal morphology, resulting in **Azo-DA/Ho** films with a radial lamellar crystal structure (Fig. 1b). By adjusting the preparation conditions of the **Azo-DA/Ho** films in various ways, we investigated the factors responsible for the dramatic change in lamellar crystal shape induced by Ho doping and the effect of the shape change on the surface properties. The results showed that the solubilities of **Azo-DA** and **Azo-DA/Ho** significantly affect the change in crystal shape and that **Azo-DA/Ho**, formed slightly in solution, acts as a pseudonucleating agent. To demonstrate the versatility of this method, we also prepared **Azo-DA/Eu, Azo-DA/Tb**, and **Azo-DA/Dy** films doped with europium (Eu), terbium (Tb), and dysprosium (Dy), respectively, instead of Ho and investigated their changes in crystal shape and effects on magnetic properties.

Experimental

Materials

N,*N*'-Dicyclohexylcarbodiimide (DCC), dichloromethane (CH_2Cl_2), and 4-dimethylamino pyridine (DMAP) were purchased from Tokyo Chemical Industry Co., Ltd. (Tokyo, Japan). Ethyl acetate, tetrahydrofuran (THF), acetone, sodium hydroxide (NaOH), holmium chloride hexahydrate ($HoCl_3 \cdot 6H_2O$), europium chloride hexahydrate ($EuCl_3 \cdot 6H_2O$), and terbium chloride hexahydrate ($TbCl_3 \cdot 6H_2O$) were obtained from Kanto Chemical Co., Inc. (Tokyo, Japan). Dysprosium chloride hexahydrate ($DyCl_3 \cdot 6H_2O$) and holmium oxide (Ho_2O_3) were obtained from FUJIFILM Wako Pure Chemical Industries, Ltd. (Osaka, Japan). All chemicals and solvents were of reagent grade and were used as received. A Millipore Simplicity UV system was used to obtain deionized water with an 18.2 MΩ·cm resistance. 5,7-Dodecadiynedioic acid and (*E*)-4-((4-(isopentyloxy)phenyl) diazenyl) phenol were synthesized according to methods reported in the literature [21].

Measurements

^{1}H and ^{13}C NMR spectra were measured on a nuclear magnetic resonance (NMR) spectrometer (AVANCE III; Bruker) at 400 MHz. Mass spectra were obtained by a mass spectrometer (Exactive; Thermo Fisher Scientific). Fourier transform infrared (FT-IR) spectra were obtained on a spectrophotometer (FT/IR-4700; JASCO). Reflection spectra were obtained on a microscopy spectrophotometer (MSV-370; JASCO). UV light irradiation was performed using a low-pressure mercury flat panel (Arc Lamp 254 nm, 11 W; Ushio). X-ray diffraction (XRD) measurements were carried out using an X-ray diffractometer (RINT-2000; Rigaku) with Cu Kα radiation (1.5418 Å). The tube current and voltage were 30 mA and 40 kV, respectively. Scanning electron microscopy (SEM) micrographs and energy-dispersive X-ray spectroscopy (EDS) maps of the samples were obtained using a scanning electron microscope (JSM-6510A; JEOL). X-ray absorption near edge structure (XANES) spectra were measured in transmission mode at BL15 of the SAGA Light Source, Kyushu Synchrotron Radiation Research Center. Optical microscope images and static contact angles were obtained using a digital microscope (VHX-500F; KEYENCE). The surface morphology of the films was analyzed using a laser microscope (VK-X1000; KEYENCE). Photographs of the samples were taken with a digital camera (OM-D E-M10; Olympus). Molecular calculations were performed with density functional theory (DFT) (method: B3LYP; basis set: 6–31 G(d)) using the Gaussian 16 program package. Magnetic properties were measured using a superconducting quantum interference device (SQUID) magnetometer (MPMS XL-5; Quantum Design). The relative electron density distribution map (EDM) profile reconstruction was performed by the method described in our previous paper [32].

Synthesis of (*E*)-12-(4-((4-(isopentyloxy) phenyl) diazenyl)phenoxy)-12-oxododeca-5,7-diynoic acid (Azo-DA)

A mixture of 5,7-dodecadiynedioic acid (1.11 g, 5.0 mmol), (*E*)-4-((4-(isopentyloxy)phenyl) dialzenyl) phenol (0.71 g, 2.5 mmol), DCC (1.03 g, 5.0 mmol), and DMAP (0.60 g, 0.9 mmol) was dissolved in THF (30 mL) under a N_2 atmosphere. The reaction mixture was stirred at room temperature. After 72 h, the solution was dried under reduced pressure. The resulting sample was purified by silica gel column chromatography (ethyl acetate/CH_2Cl_2 = 1/7), giving rise to **Azo-DA** (0.54 g, 1.1 mmol) as a yellow solid in 31% yield. ^{1}H NMR (400 MHz, $CDCl_3$, δ): 0.98 (d, $J = 6.5$ Hz, 6H), 1.72 (q, $J = 6.8$ Hz, 2H), 1.86 (m, 3H), 1.99 (q, $J = 7.2$ Hz, 2H), 2.38 (t, $J = 6.9$ Hz, 2H), 2.45 (t, $J = 6.9$ Hz, 2H), 2.51 (t, $J = 7.4$ Hz, 2H), 2.75 (t, $J = 7.4$ Hz, 2H), 4.08 (t, $J = 6.8$ Hz, 2H), 7.00 (d, $J = 9.0$ Hz, 2H), 7.23 (d, $J = 9.0$ Hz, 2H), 7.90 (m, 4H); ^{13}C NMR (100 MHz, $CDCl_3$, δ): 18.57 (CH_2),18.64 (CH_2), 22.61 (CH_3), 23.18 (CH_2), 23.33 (CH_2), 25.05 (CH), 32.58 (CH_2), 33.03 (CH_2), 37.89 (CH_2), 66.18 (C≡C), 66.30 (C≡C), 66.77 (CH_2), 76.24 (C≡C), 76.41 (C≡C), 114.73 (Ar, C-H), 122.14 (Ar, C-H), 123.70 (Ar, C-H), 124.80 (Ar, C-H), 146.73 (Ar), 150.40 (Ar), 152.02 (Ar), 161.77 (Ar), 171.27 (C=O), 178.84 (C=O); ESI(+)-MS calcd. for $C_{29}H_{32}O_5N_2Na$ ($[M+Na]^+$): 511.2203; found: 511.2199.

Preparation of Azo-DA films

The synthesized **Azo-DA** was dissolved in an acetone/H_2O mixture at 80 °C and left at room temperature for recrystallization. The resulting crystals were deposited on filter paper ($\Phi = 8$ mm) by suction filtration to obtain an **Azo-DA** film (film thickness: approximately 100 μm) (Fig. S1).

Preparation of Azo-DA/Ho films

Typical Ho coordination conditions are shown below. For the detailed coordination conditions used in each experiment, refer to the figure captions. $HoCl_3 \cdot 6H_2O$ (0.02 g, 0.05 mmol), THF (3.33 mL), distilled water (6.67 mL), and 0.1 M NaOH aq. (0.03 mL) were added to the sample bottle and cooled in an incubator at 15 °C. The **Azo-DA** film (3.0 mg) was then immersed in the solution in the sample bottle (Fig. S2). After 5 days, the samples were washed three times with distilled water and three times with acetone and dried under vacuum to obtain **Azo-DA/Ho** films. **Azo-DA/Eu, Azo-DA/Tb**, and **Azo-DA/Dy** films were prepared by using $EuCl_3 \cdot 6H_2O$, $TbCl_3 \cdot 6H_2O$, and $DyCl_3 \cdot 6H_2O$, respectively, instead of $HoCl_3 \cdot 6H_2O$.

Results and discussion

Azo-DA, which has a branched azobenzene moiety on one side of DA and a carboxy group on the other side, was synthesized by the reaction shown in Fig. S3, and its structure was confirmed by NMR and MS analysis (Figs. S4 and S5). In accordance with previous methods, **Azo-DA** was recrystallized in a mixed solvent of acetone and H_2O [21]. The crystals generated by suction filtration were deposited on filter paper and then removed, resulting in an **Azo-DA** film with a thickness of approximately 100 μm, as calculated from the cross-sectional SEM image (Fig. S6a). While the film thickness can be controlled by changing the amount of sample used for deposition, the film cannot be peeled off from the filter paper if it is less than 100 μm [21]. Therefore, we performed subsequent experiments using a 100 μm thick **Azo-DA** film that forms a

freestanding film. The **Azo-DA/Ho** film was then prepared by immersing the **Azo-DA** film in a Ho solution, which consisted of $HoCl_3 \cdot 6H_2O$, a THF/H_2O mixture, and NaOH (Fig. S2). The FT-IR spectra of **Azo-DA/Ho** films immersed for 1, 3, and 5 days in a Ho solution at 15 °C, which was used to inhibit solvent evaporation, are shown in Fig. 2a. The peak observed at 1690 cm^{-1} in the IR spectrum of the **Azo-DA** film, which originates from the C=O stretching vibration of the carboxy group of **Azo-DA**, gradually decreased with increasing immersion time in the Ho solution. On the other hand, a new peak at 1533 cm^{-1} was observed after Ho immersion, indicating that Ho forms a complex with carboxy groups [33, 34]. After 5 days of immersion, all the carboxy groups of the **Azo-DA** film were coordinated with Ho. The complexation of Ho to **Azo-DA** was evaluated by SEM–EDS mapping (Fig. S7). As shown in Fig. 2b, the elemental mapping data for carbon (C), nitrogen (N), oxygen (O), and Ho are consistent with the SEM image of the **Azo-DA/Ho** film, indicating that the **Azo-DA/Ho** film uniformly contains Ho. XANES measurements were used to investigate the valence of Ho in the **Azo-DA/Ho** film. In the XANES spectra of the reference sample, Ho_2O_3, and the **Azo-DA/Ho** film, a peak was observed at 8073 eV in both cases (Fig. 2c). This indicates that the Ho in the **Azo-DA/Ho** film exists in the Ho^{3+} state, as in Ho_2O_3, suggesting that one Ho is coordinated to the carboxy group of three molecules of **Azo-DA** [35, 36].

The microscopic crystal structures of the **Azo-DA** and **Azo-DA/Ho** films were evaluated via XRD (Fig. 3a and S8). Both films showed equally spaced diffraction peaks, suggesting the formation of an ordered lamellar layer structure. The following Bragg equation (Eq. 1) was used to calculate the layer spacing d of the prepared films:

$$d = m\lambda/(2\sin\theta) \quad (1)$$

where m is the diffraction order, λ is the X-ray wavelength, and θ is the angle between the crystal plane and the incident X-ray. The d values of the **Azo-DA** and **Azo-DA/Ho** films are 54.0 and 55.2 Å, respectively, indicating that the interlayer spacing is widened by Ho coordination. In the **Azo-DA/Ho** film, in addition to peaks originating from the lamellar layer, multiple peaks, presumably π-π stacking of azobenzene moieties, were observed in the $2\theta = 20$–$23°$ region. Since the molecular length of **Azo-DA** determined by DFT calculations is 30.3 Å (Fig. S9a), which is considerably smaller than the interlayer spacing of 54.0 Å in the **Azo-DA** film, it is assumed that **Azo-DA** with carboxyl groups is dimerized within the layer [37]. DFT calculation-based structural optimization of the **Azo-DA** dimer with a dimerized carboxylic acid moiety yielded a linear molecular shape (molecular length: 53.5 Å) (Fig. S9b). Figure 3b shows a schematic diagram of the proposed lamellar structure consisting of **Azo-DA** dimers with an EDM profile created from the peak positions and peak areas obtained from XRD measurements of the **Azo-DA** film. The assumed **Azo-DA/Ho** lamellar structure is also illustrated in the EDM profile of **Azo-DA/Ho** for an ionic radius of 0.901 nm when Ho is 6-coordinated [38]. From these diagrams, the inclination angles of the DA moieties within the **Azo-DA** and **Azo-DA/Ho** films were calculated to be approximately 66° and 39°, respectively.

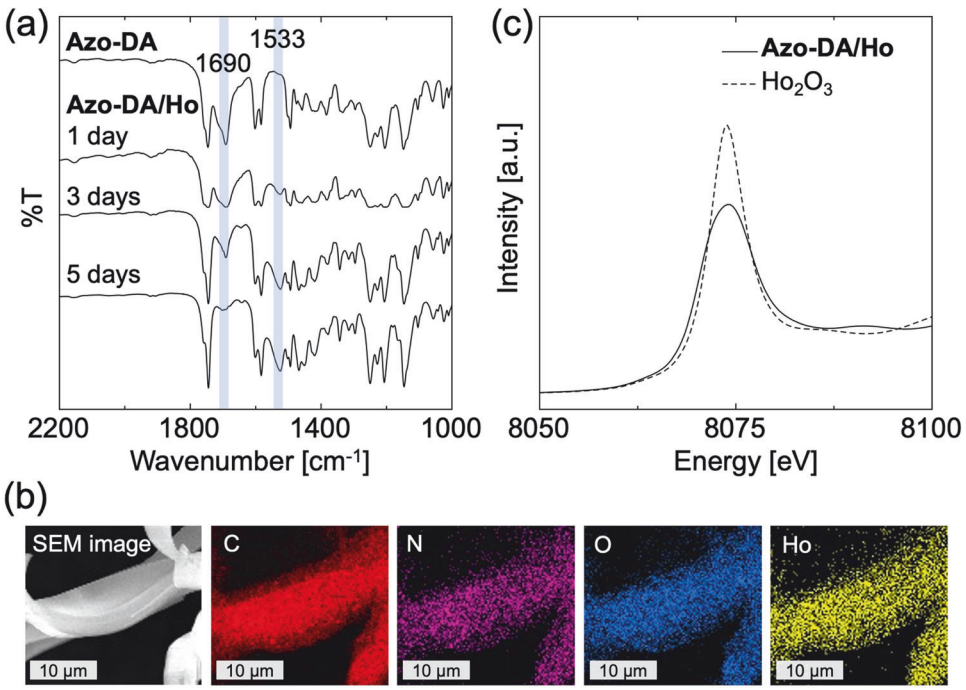

Fig. 2 **a** FT-IR spectra of **Azo-DA** and **Azo-DA/Ho** films immersed in Ho solution for 1, 3, and 5 days. **b** SEM image and EDS mapping data for **Azo-DA/Ho**. **c** XANES spectra for **Azo-DA/Ho** and the reference sample Ho_2O_3

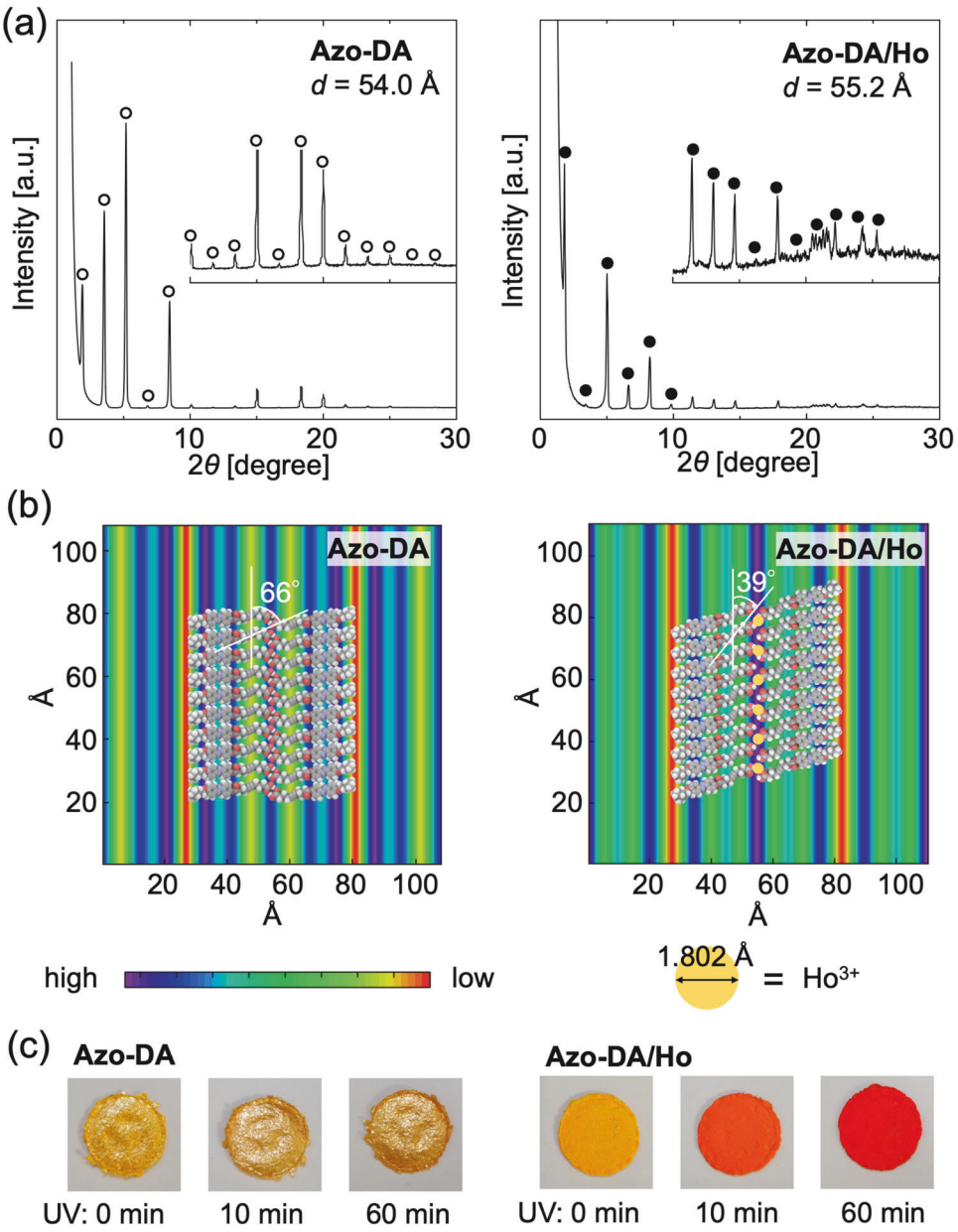

Fig. 3 **a** XRD profiles of the **Azo-DA** and **Azo-DA/Ho** films. The white and black circles indicate peaks attributed to the lamellar structure. The numbers in the figure indicate the spacing *d* of the lamellar layers. **b** EDM profiles of the **Azo-DA** and **Azo-DA/Ho** films. The proposed alignment model of the molecule is shown in the EDM profile. The numbers in the schematic indicate the inclination angle of the DA moiety. **c** Photographs of **Azo-DA** and **Azo-DA/Ho** films exposed to 254 nm UV light

The inclination angle of the DA moiety is closely related to the progress of solid-phase polymerization by photoirradiation; polymerization is most likely to progress when the inclination angle is 45° [39]. **Azo-DA** and **Azo-DA/Ho** films were irradiated with UV light at 254 nm to examine their polymerization behavior (Fig. 3c). Under UV irradiation, for the **Azo-DA** film with a high inclination angle of 66°, the original golden color was maintained, and almost no change in color was observed. On the other hand, UV irradiation of the **Azo-DA/Ho** film, whose inclination angle is close to the optimum angle for polymerization, causes an apparent color change from yellow to orange to red, indicating elongation of the conjugation length due to the polymerization of the DA moieties. The polymerization behavior of the **Azo-DA** and **Azo-DA/Ho** films indicated the validity of the obtained inclination angles. While PDA is known as a polymer with thermochromism, **Azo-DA** and **Azo-DA/Ho** films irradiated with 254 nm UV light showed almost no color change after heating at 30–100 °C (Fig. S10a). Furthermore, no color change was observed in the **Azo-DA** or **Azo-DA/Ho** films after UV irradiation at 365 nm, where isomerization of the azobenzene moiety progresses (Fig. S10b). These results suggest that molecular motion is suppressed within the densely packed lamellar structure.

The appearance of the **Azo-DA** films changed significantly before and after Ho coordination (Fig. 3c). The **Azo-DA** film exhibited a golden luster, whereas the

Azo-DA/Ho film had a matte texture. In the reflection spectra of the **Azo-DA** and **Azo-DA/Ho** films, the spectral shapes are almost the same (Fig. 4a). The spectra are observed at the position corresponding to the yellow reflection, which is attributed to the absorption of azobenzene. On the other hand, a significant difference in reflectance was observed, with the maximum reflectance of approximately 24% for the **Azo-DA** film significantly reduced to approximately 6% for the **Azo-DA/Ho** film. As shown in Fig. 1b, SEM observation of the **Azo-DA** film shows that the plate-like crystals are stacked to form a smooth surface, consistent with the surface morphology of the **DAzo-DA** film, which has a golden luster, as reported previously. Interestingly, the SEM image of the **Azo-DA/Ho** film shows microscopic irregularities over the entire surface (Fig. 1b). One day after immersion in the Ho solution, the plate-like crystals observed in the **Azo-DA** film were completely absent. Instead, many hierarchical structures were observed, consisting of urchin-like crystals that formed on a spherical dome with a diameter of approximately 100 µm. As the immersion time increased, the crystals grew further, and after 5 days, a structure of radially growing crystals with a width of approximately 5 µm was observed. The thicknesses of the **Azo-DA** and **Azo-DA/Ho** (5 days) films calculated by cross-sectional SEM measurements were approximately 100 µm (Fig. S6b). The effect of gravity on crystal growth was investigated. Ho doping was performed on **Azo-DA** films wired vertically to the bottom of a bottle. The SEM image of the film surface after Ho doping showed the presence of radial crystals with almost the same structure as above (Fig. S11). Therefore, gravity seems to have little effect on crystal growth in this system. The surfaces of the films before and after immersion in the Ho solution were observed with a laser microscope (Fig. 4b). The root mean square height (Sq), an index of surface roughness, was 17.4 µm for the **Azo-DA** film and 30.4 µm for the **Azo-DA/Ho** film, indicating that a rougher surface was formed by Ho coordination. These results suggest that the change in texture before and after Ho coordination is caused by a change in light reflection properties caused by the difference in surface roughness; the metallic luster of the **Azo-DA** film is due to specular reflection from a smooth surface, while the matte texture of the **Azo-DA/Ho** film is due to diffuse reflection from a rough surface [40].

The dramatic morphological change in the film surface due to the coordination of Ho resulted in changes not only in the appearance of the film but also in its surface properties. The contact angles were measured by dropping 2 µL of water on the resulting films (Fig. 5a). The water contact angle of the **Azo-DA** film, which was approximately 75°, changed to approximately 148° for the **Azo-DA/Ho** film, indicating a dramatic improvement in water repellency due to Ho coordination. The change in contact angle when the inclined film was measured is shown in Fig. 5a. The **azo-DA** film failed to retain water droplets. However, the **Azo-DA/Ho** film was found to maintain water repellency at any angle. Furthermore, the so-called petal effect, in which water droplets remain on the surface even when the film is rotated 180°, was also observed, indicating that in addition to water repellency, the film has excellent water droplet adsorption properties. Surfaces with both water repellency and adsorption properties are abundant in nature, and a typical example is the surface of a rose petal, which consists of hierarchical micro- and nanostructures [41, 42]. On the surface of the **Azo-DA/Ho** film, there is a hierarchical structure with crystals approximately 5 µm in width growing radially on a dome structure approximately 100 µm in width (*vide supra*). When the **Azo-DA/Ho** film sandwiched between glass substrates was pressed to flatten the surface, the contact angle of the water decreased to approximately 112° (Fig. S12). This indicates that the surface properties of the **Azo-DA/Ho** film are not due to changes in surface free energy derived from the elemental composition of the material surface but from its hierarchical structure. **Azo-DA/Ho** films exhibited high water repellency and adsorption due to the Cassie–Baxter state, which retains air between the water droplets and the hierarchical structure (Fig. 5b) [43–45].

To explore the factors that dramatically change the crystal shape, which has a significant impact on the surface properties, we comprehensively examined the coordination conditions of Ho. First, the effect of the Ho concentration on the crystal shape was investigated (Fig. 6a). **Azo-DA/Ho** films were prepared by adding 0.2–20 equivalents of $HoCl_3 \cdot 6H_2O$ to **Azo-DA**. Under 0.2 eq. of $HoCl_3 \cdot 6H_2O$, little change in the crystal shape was observed. On the other hand, at more than 1 eq., radial crystal growth was observed, and a significant change in crystal shape was observed. As mentioned above, one Ho atom would coordinate with three molecules of **Azo-DA**, which has a terminal carboxyl group, indicating that at least 0.3 eq. of $HoCl_3 \cdot 6H_2O$ is required for **Azo-DA**. IR measurements corroborated this observation: the IR spectrum of the film prepared with 0.2 eq. of $HoCl_3 \cdot 6H_2O$ showed a peak at 1690 cm^{-1} originating from C=O stretching vibrations, indicating residual uncoordinated **Azo-DA**, while under conditions with more than 1 eq., all the **Azo-DA** was shown to be coordinated with Ho (Fig. S13). It should be noted that increasing the amount of $HoCl_3 \cdot 6H_2O$ decreases the width of the radially growing crystals: crystals with a width of approximately 12 µm obtained under 1.0 eq. of $HoCl_3 \cdot 6H_2O$ were reduced to approximately 9 µm and 3 µm under 10 and 20 eq. of $HoCl_3 \cdot 6H_2O$, respectively. This probably increased the number of **Azo-DA/Ho** nuclei produced by the increased amount of $HoCl_3 \cdot 6H_2O$, resulting in a decrease in the degree of crystal growth from the nuclei and

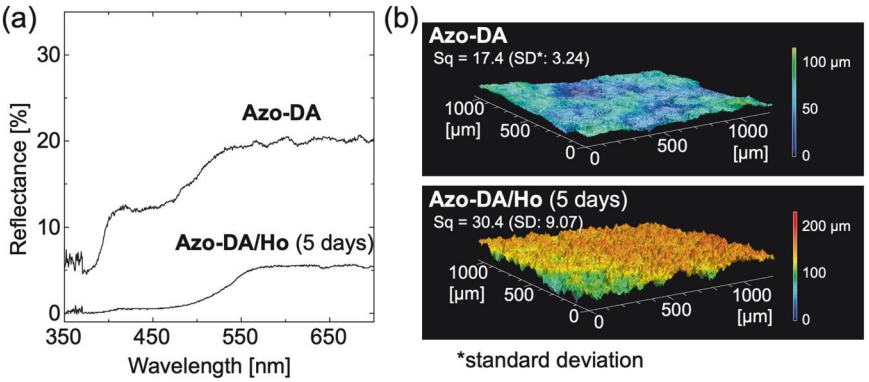

Fig. 4 **a** Reflection spectra of the **Azo-DA** and **Azo-DA/Ho** films. **b** Laser microscopic images of the **Azo-DA** and **Azo-DA/Ho** films

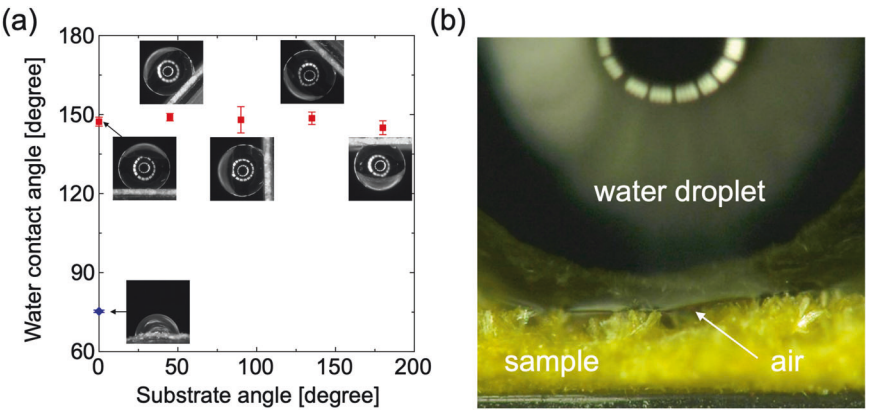

Fig. 5 **a** Water contact angles for **Azo-DA** and **Azo-DA/Ho** films measured at different angles. The water contact angle values are the average of three measurements. **b** Digital microscope image of the **Azo-DA/Ho** film surface with a water droplet

a decrease in crystal width. In this experiment, the coordination of Ho was performed under static conditions without stirring to avoid physical destruction of the **Azo-DA** film. Using an excess amount of $HoCl_3 \cdot 6H_2O$ (10 eq.), we then examined the role of NaOH. **Azo-DA/Ho** films were prepared under conditions where dramatic crystal shape changes were observed, excluding only NaOH (Fig. S14a). Although the crystal surface shape was disrupted, no radial crystal growth was observed, and IR measurements indicated the presence of a large amount of residual **Azo-DA** (Fig. S14b). The carboxyl group must be sufficiently ionized to coordinate with the metal. Therefore, under acidic conditions without NaOH, coordination between Ho and the carboxyl group did not occur, and crystal growth was likely inhibited.

The solvent composition is also an essential parameter during metal coordination. In this experiment, Ho was coordinated in a THF/H_2O solution, which is a mixture of a good solvent (THF) and a poor solvent (H_2O) at any ratio for **Azo-DA** production. As shown in Fig. 6b, the change in crystal shape became more pronounced as the proportion of THF increased, with characteristic radial crystal growth observed under THF/H_2O = 4/10 and 5/10. When the THF/H_2O ratio was 6/10, the proportion of the good solvent was too high, and **Azo-DA** dissolved quickly, causing the collapse of the film structure. Interestingly, when the experiment was performed without the addition of $HoCl_3 \cdot 6H_2O$ at THF/H_2O = 5/10, where the crystal structure changed dramatically while maintaining the film shape, the added **Azo-DA** film collapsed instantly. The UV–vis spectra of the residual solution after immersing the **Azo-DA** film for 5 days in the absence or presence of $HoCl_3 \cdot 6H_2O$ are shown in Fig. 6c. In the absence of $HoCl_3 \cdot 6H_2O$, where the **Azo-DA** film was fully dissolved, a significant absorption band at approximately 350 nm derived from **Azo-DA** was observed. On the other hand, in the presence of $HoCl_3 \cdot 6H_2O$, absorption derived from **Azo-DA** was hardly observed despite the conditions under which the **Azo-DA** film dissolves. Furthermore, SEM images of the film after 5 days of immersion in THF/H_2O = 4/10 without $HoCl_3 \cdot 6H_2O$, in which the film structure was maintained, showed that the **Azo-DA** plate-like crystals that formed the film dissolved from the surface (Fig. S15). These results suggested that at THF/H_2O = 5/10, the **Azo-DA** film dissolves from the surface and recrystallizes by forming a complex with Ho in the solution phase. SEM images taken in the early stages of Ho coordination support this conclusion (Fig. 6d). In the SEM image of the **Azo-DA** film after 10 min of immersion in Ho solution, some plate-like **Azo-DA** crystals remained on the surface, and numerous small aggregates, probably deposited by the **Azo-DA/Ho** generated in the solution phase, were observed on top of the film. After 1 h, the percentage of

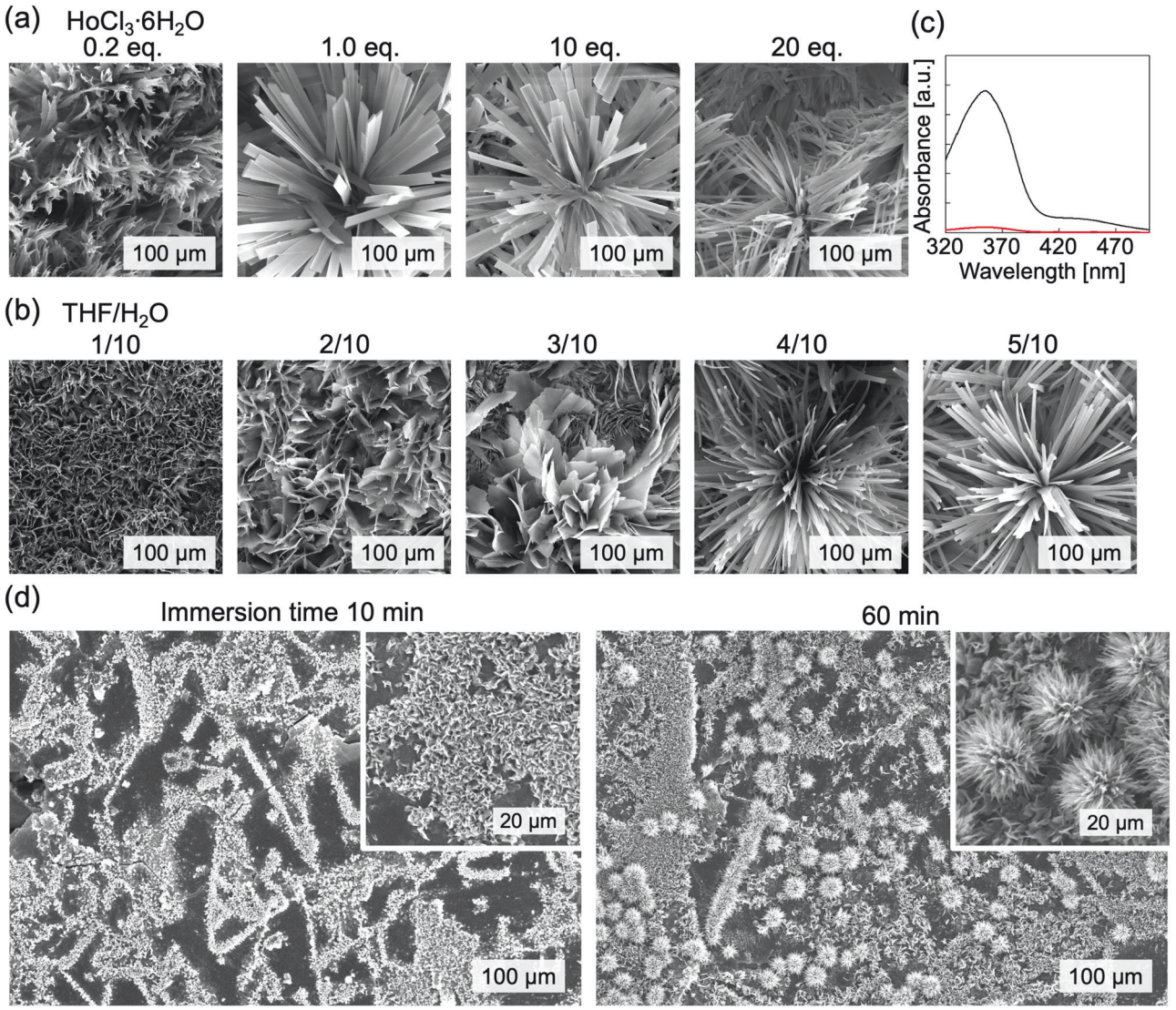

Fig. 6 **a** SEM images of film surfaces prepared by varying the concentration of $HoCl_3 \cdot 6H_2O$. **b** SEM images of film surfaces prepared by varying the ratio of THF to H_2O. **c** UV–vis spectra of the residual solution after immersion of the **Azo-DA** film in the absence (black line) and presence (red line) of $HoCl_3 \cdot 6H_2O$ for 5 days. **d** SEM images of the film surface during the initial process of making the **Azo-DA/Ho** film (after 10 and 60 min of immersion). The inset shows a magnified view

plate-like crystals decreased, and some distinct urchin-like crystals, presumably composed of **Azo-DA/Ho** aggregates, appeared. Further immersion in the Ho solution resulted in the growth of urchin-like crystals, and the formation of a film was entirely covered by the characteristic radial crystals, as shown in Fig. 1b.

Figure 7 shows the proposed **Azo-DA/Ho** film formation mechanism. When plate-like **Azo-DA** lamellar crystals obtained by recrystallization are immersed in a Ho solution, a THF/H_2O mixture in which $HoCl_3$ and NaOH are dissolved, **Azo-DA** is slightly eluted from the crystal surface due to the effect of THF, which is a good solvent. Slightly dissolved **Azo-DA** molecules encounter $HoCl_3$ in the solution phase and form a complex. The low solubility of the **Azo-DA/Ho** complex caused it to crystallize again and deposit on the surface of the lamellar crystals, forming **Azo-DA/Ho** nuclei. The dissolution of **Azo-DA** from plate-like crystals and the assembly of **Azo-DA/Ho** by recrystallization of the generated nuclei proceeded, resulting in the appearance of urchin-like crystals, as shown in Fig. 1b. The reason for the formation of urchin-like structures has yet to be determined. Nevertheless, the tendency of lamellae to grow radially in the presence of a nucleating agent has been discussed in several papers [46, 47], possibly because of the radial elongation of the lamellae when **Azo-DA/Ho** assembles into the nucleus, which acts as a pseudonucleating agent, resulting in urchin-like growth. Further assembly of **Azo-DA/Ho** into an urchin-like structure eventually results in a film covered with radial crystals. Note that the film structure is maintained after the formation

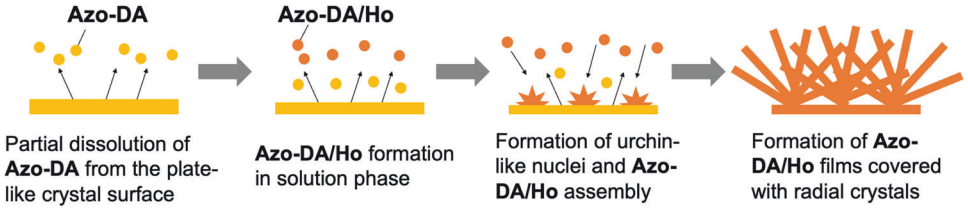

Fig. 7 Schematic of the formation of an **Azo-DA/Ho** film with radial crystals on the surface via urchin-like crystals from a plate-like **Azo-DA** lamellar film

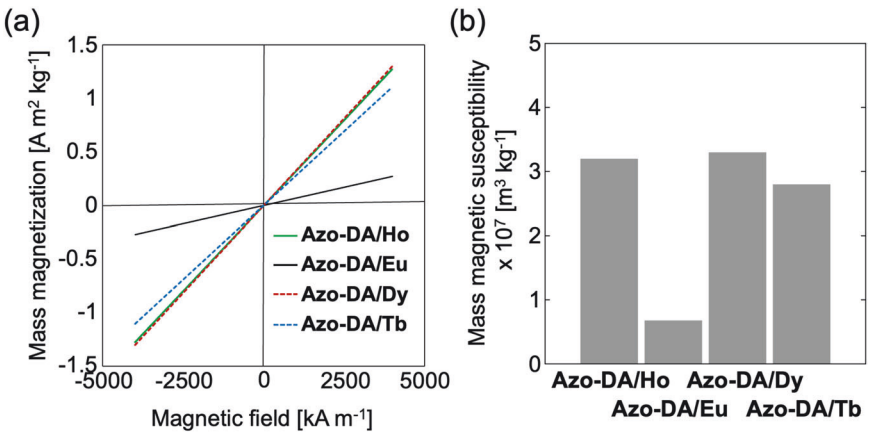

Fig. 8 **a** Mass magnetic susceptibility results for the prepared **Azo-DA/Ho, Azo-DA/Eu, Azo-DA/Tb**, and **Azo-DA/Dy** films. **b** Results for the mass susceptibilities of the **Azo-DA/Ho, Azo-DA/Eu, Azo-DA/Tb**, and **Azo-DA/Dy** films calculated from the slope of the plot in (**a**)

of the **Azo-DA/Ho** film. Fig. S16 shows an SEM image of the film surface prepared by immersing half of the **Azo-DA** film in the Ho solution; radial crystal formation is observed only on the surface of the portion immersed in the Ho solution, indicating that the film structure was not destroyed. This indicates that the partially dissolved **Azo-DA** reassembled on the nearby film surface after becoming **Azo-DA/Ho** in the solution phase.

To demonstrate the versatility of this method, **Azo-DA/Eu, Azo-DA/Tb**, and **Azo-DA/Dy** films were prepared by coordinating Eu, Tb, and Dy, respectively, instead of Ho. According to the IR spectra of the **Azo-DA/Eu, Azo-DA/Tb**, and **Azo-DA/Dy** films, the C=O stretching peak shifts from approximately 1690 cm^{-1} to 1530 cm^{-1}, indicating that each element is coordinated (Fig. S17). XRD measurements showed that the **Azo-DA/Eu, Azo-DA/Tb**, and **Azo-DA/Dy** films also formed lamellar structures (Fig. S18). The coordination of Eu, Tb, and Dy increased the layer spacing from 54.0 Å in the **Azo-DA** film to 55.5, 55.7, and 55.0 Å, respectively. SEM images of the film surfaces showed radial crystal growth similar to that of the Ho-coordinated film (Fig. S19a). **Azo-DA/Tb** and **Azo-DA/Dy** had narrower crystal widths, whereas **Azo-DA/Eu** and **Azo-DA/Ho** had comparable crystal widths. Although the detailed reason for the change in crystal width depending on the type of lanthanide is not yet known, lanthanide doping in this system was performed by placing the **Azo-DA** film in a lanthanide solution. Therefore, the solubility of **Azo-DA** after lanthanide doping and the convection of the solution may have affected the crystal growth and width. All the films changed from the metallic luster observed in the **Azo-DA** film to a matte appearance and exhibited improved water repellency (Fig. S20). SEM–EDS mapping clearly revealed the doping of each element, indicating that this method is not specific to Ho but is applicable to a wide range of lanthanide elements (Fig. S19b). Since the magnetic properties of lanthanide elements depend on their type [48, 49], we investigated whether the selection of doping elements could tune the magnetic properties of the resulting films. The mass magnetic susceptibility of the prepared films with each element coordinated was determined by SQUID measurements. As shown in Fig. 8a, a plot through the origin is obtained in all the cases, indicating the paramagnetic nature of the resulting films. The mass susceptibilities of the **Azo-DA/Ho, Azo-DA/Eu, Azo-DA/Tb**, and **Azo-DA/Dy** films calculated from the slope of the plot were 3.2×10^{-7}, 0.68×10^{-7}, 3.3×10^{-7}, and 2.8×10^{-7} ($m^3\,kg^{-1}$), respectively (Fig. 8b). The order of the obtained values of the mass susceptibilities of films prepared with each element is consistent with a previous report comparing the mass susceptibilities of polymer particles doped with the same amount of each element. In the coordination of lanthanides to **Azo-DA** lamellar films, it was shown that while specific crystal shape changes occur regardless of the type of lanthanide, the magnetic properties can be tuned by the choice of lanthanide.

Conclusion

In conclusion, we demonstrated that doping lanthanides into plate-like lamellar crystals of **Azo-DA** causes reorganization

of the lamellar structure, dramatically changing the crystal morphology. When plate-like lamellar crystals of **Azo-DA** were immersed in Ho solution, A**zo-DA/Ho**, which was slightly formed by complexation in the solution phase during Ho doping, acted as a pseudonucleating agent to form nuclei. Dissolution of **Azo-DA** from the plate-like crystals and assembly of **Azo-DA/Ho** by recrystallization of the generated nuclei proceeded, forming urchin-like crystals; ultimately, radially growing **Azo-DA/Ho** lamellar crystals were formed. The morphological changes in the lamellar crystal films were also found to have a significant effect on the surface properties of the films, such as their appearance and water repellency. While most PDA studies have focused on imparting chromism properties to PDA, we have successfully induced rearrangements and morphological changes in lamellar crystals by lanthanide doping. This method is versatile enough to use not only Ho but also other lanthanide elements, and the magnetic properties of the obtained samples are controlled by the type of doping element. The newly developed method of changing crystal morphology based on ion doping into DA lamellar crystals is expected to contribute to the fundamentals of DA chemistry and advance the surface functionalization of lamellar crystal films.

Acknowledgements MK acknowledges the support of the Japan Society for the Promotion of Science (JSPS) KAKENHI (Grant Nos. JP20H02793 and JP23H02018) and the Shorai Foundation for Science and Technology. HW acknowledges the support of the MEXT Quantum Leap Flagship Program (MEXT Q-LEAP, Grant No. JPMXS0118068681) and JSPS KAKENHI (Grant No. JP19H05824). XANES measurements were performed at BL15 of the SAGA Light Source (proposal no. 2110123 F). We thank Mr. R. Takahashi, Mr. Y. Tani (University of Hyogo), Dr. H. Setoyama, and Dr. E. Magome (Kyushu Synchrotron Light Research Center), who cooperated with the XANES measurements. We thank Ms. M. Moriya (Chiba University) for developing the EDM program. We used the computer server of the Digital Transformation Promotion Council of Chiba University for the computational simulations. We thank Prof. T. Ohkubo (Chiba University) for establishing the server access system.

Compliance with ethical standards

Conflict of interest The authors declare no competing interests.

Publisher's note Springer Nature remains neutral with regard to jurisdictional claims in published maps and institutional affiliations.

References

1. An YJ, Kajiwara T, Padermshoke A, Nguyen TV, Feng SN, Masunaga H, et al. Photooxidative degradation and fragmentation behaviors of oriented isotactic polypropylene. Polym J. 2024. https://doi.org/10.1038/s41428-023-00876-4.
2. Tadokoro D, Konishi T, Fukao K, Miyamoto Y. Lamellar crystallization of poly(trimethylene terephthalate). Polym J. 2023;55:775–83.
3. Yamamoto H, Yoshioka T, Funaki K, Masunaga H, Woo EM, Tashiro K. Synchrotron x-ray-analyzed inner structure of polyethylene spherulites and atomistic simulation of a trigger of the lamellar twisting phenomenon. Polym J. 2023;55:27–43.
4. Takashina Y, Hoshino K. Effect of π-π interaction-induced secondary doping on the gold-like luster of oligo (3-methoxythiophene) cast films. Polym J. 2019;51:591–9.
5. Reiter G. Some unique features of polymer crystallisation. Chem Soc Rev. 2014;43:2055–65.
6. Majumder S, Busch H, Poudel P, Mecking S, Reiter G. Growth kinetics of stacks of lamellar polymer crystals. Macromolecules. 2018;51:8738–45.
7. Liu YT, Yin LX, Zhao HR, Song GK, Tang FM, Wang LL, et al. Lamellar and fibrillar structure evolution of poly(ethylene terephthalate) fiber in thermal annealing. Polymer. 2016;105:157–66.
8. Amada K, Ishizaki M, Kurihara M, Matsui J. Self-assembly and -cross-linking lamellar films by nanophase separation with solvent-induced anisotropic structural changes. ACS Omega. 2022;7:16778–84.
9. Poudel P, Chandran S, Majumder S, Reiter G. Controlling polymer crystallization kinetics by sample history. Macromol Chem Phys. 2018;219:1700315.
10. Majumder S, Poudel P, Zhang H, Xu J, Reiter G. A nucleation mechanism leading to stacking of lamellar crystals in polymer thin films. Polym Int. 2020;69:1058–65.
11. Mamun A. Retardation of the growth rate of the basal and overgrown lamellar crystals of PCL/PVME miscible binary blends with thickness confinement. Polym J. 2022;54:653–65.
12. Liu W, Yin HM, Shi A, Sun WJ, Wu DW, Huang SS, et al. Surface-directed self-epitaxial crystallization of poly(ε-caprolactone) from isotropic to highly orientated lamellae. Macromolecules. 2020;53:1736–44.
13. Xie Q, Chang XH, Qian Q, Pan PJ, Li CY. Structure and morphology of poly(lactic acid) stereocomplex nanofiber shish kebabs. ACS Macro Lett. 2020;9:103–7.
14. Matsumoto A. Polymer structure control based on crystal engineering for materials design. Polym J. 2003;35:93–121.
15. Reppy MA, Pindzola BA. Biosensing with polydiacetylene materials: structures, optical properties and applications. Chem Commun. 2007:4317–38. https://doi.org/10.1039/B703691D.
16. Ikeshima M, Mamada M, Minami T, Tokito S, Okada S. Synthesis and solid-state polymerization of diacetylene derivatives directly substituted with a phenylcarbazole moiety. Polym J. 2016;48:1013–8.
17. Oaki Y. Morphology design of crystalline and polymer materials from nanoscopic to macroscopic scales. Bull Chem Soc Jpn. 2017;90:776–88.
18. Mukai M, Kogiso M, Aoyagi M, Asakawa M, Shimizu T, Minamikawa H. Supramolecular nanofiber formation from commercially available arginine and a bola-type diacetylenic diacid hydrogelation. Polym J. 2012;44:646–50.
19. Sada K, Takeuchi M, Fujita N, Numata M, Shinkai S. Post-polymerization of preorganized assemblies for creating shape-controlled functional materials. Chem Soc Rev. 2007;36:415–35.

20. Sun XM, Chen T, Huang SQ, Li L, Peng HS. Chromatic polydiacetylene with novel sensitivity. Chem Soc Rev. 2010;39:4244–57.
21. Kojima Y, Kishikawa K, Ichikawa S, Matsui J, Hirai K, Kondo Y, et al. Stimuli-responsive biomimetic metallic luster films using dye absorption and specular reflection from layered microcrystals. ACS Appl Polym Mater. 2021;3:1819–27.
22. Fang SS, Leung SYL, Li YG, Yam VWW. Directional self-assembly and photoinduced polymerization of diacetylene-containing platinum(ii) terpyridine complexes. Chem Eur J. 2018;24:15596–602.
23. Xu R, Schweizer B, Frauenrath H. Soluble poly(diacetylene)s using the perfluorophenyl-phenyl motif as a supermolecule synthon. J Am Chem Soc. 2008;130:11437–45.
24. Li Z, Fowler FW, Lauher JW. Weak interactions dominating the supramolecular self-assembly in a salt: a designed single-crystal-to-single-crystal topochemical polymerization of a terminal aryldiacetylene. J Am Chem Soc. 2009;131:634–43.
25. Yoon B, Lee J, Park IS, Jeon S, Lee J, Kim JM. Recent functional material based approaches to prevent and detect counterfeiting. J Mater Chem C. 2013;1:2388–403.
26. Ono N, Seishima R, Okabayashi K, Imai H, Fujii S, Oaki Y. Stimuli-responsive sponge for imaging and measuring weak compression stresses. Adv Sci. 2023;10:e2206097.
27. Chen XQ, Zhou GD, Peng XJ, Yoon J. Biosensors and chemosensors based on the optical responses of polydiacetylenes. Chem Soc Rev. 2012;41:4610–30.
28. Takajo D, Okawa Y, Hasegawa T, Aono M. Chain polymerization of diacetylene compound multilayer films on the topmost surface initiated by a scanning tunneling microscope tip. Langmuir. 2007;23:5247–50.
29. Kim Y, Aoki K, Fujioka M, Nishii J, Tamaoki N. Pressure-induced transition of bisamide-substituted diacetylene crystals from nonphotopolymerizable to photopolymerizable state. ACS App Mater Interfaces. 2018;10:36407–14.
30. Kajiwara T. A holmium(iii)-based single-molecule magnet with pentagonal-bipyramidal geometry. Angew Chem Int Ed. 2017;56:11306–8.
31. Kohaku K, Inoue M, Kanoh H, Taniguchi T, Kishikawa K, Kohri M. Full-color magnetic nanoparticles based on holmium-doped polymers. ACS Appl Polym Mater. 2020;2:1800–6.
32. Moriya M, Kohri M, Kishikawa K. Chiral self-sorting and the realization of ferroelectricity in the columnar liquid crystal phase of an optically inactive *N*,*N*'-diphenylurea derivative possessing six (±)-citronellyl groups. ACS Omega. 2021;6:18451–7.
33. Cao FY, Huang TC, Wang YF, Liu F, Chen LM, Ling J, et al. Novel lanthanide-polymer complexes for dye-free dual modal probes for MRI and fluorescence imaging. Polym Chem. 2015;6:7949–57.
34. Kohri M, Yanagimoto K, Kohaku K, Shiomoto S, Kobayashi M, Imai A, et al. Magnetically responsive polymer network constructed by poly(acrylic acid) and holmium. Macromolecules. 2018;51:6740–5.
35. Asakura H, Shishido T, Teramura K, Tanaka T. Local structure and L_1- and L_3-edge X-ray absorption near edge structure of late lanthanide elements (Ho, Er, Yb) in their complex oxides. J Phys Chem C. 2015;119:8070–7.
36. Fujita Y, Kohaku K, Komiyama N, Ujiie K, Masu H, Kojima T, et al. Colorless magnetic colloidal particles based on an amorphous metal-organic framework using holmium as the metal species. ChemNanoMat. 2022;8:e202200078.
37. Oaki Y, Ishijima Y, Imai H. Emergence of temperature-dependent and reversible color-changing properties by the stabilization of layered polydiacetylene through intercalation. Polym J. 2018;50:319–26.
38. Ahmad D, Ali A, Abbas Z, Zaman A, Alsuhaibani AM, Tirth V, et al. Structural, optical and dielectric properties of holmium-doped nickel-cadmium ferrite nanoparticles synthesized by sol-gel auto-combustion method. Crystals. 2023;13:495.
39. Enkelmann V. Structural aspects of the topochemical polymerization of diacetylenes. Adv Polym Sci. 1984;63:91–136.
40. Kohri M, Nannichi Y, Taniguchi T, Kishikawa K. Biomimetic non-iridescent structural color materials from polydopamine black particles that mimic melanin granules. J Mater Chem C. 2015;3:720–4.
41. Feng L, Zhang YA, Xi JM, Zhu Y, Wang N, Xia F, et al. Petal effect: a superhydrophobic state with high adhesive force. Langmuir. 2008;24:4114–9.
42. Archer RJ, Becher-Nienhaus B, Dunderdale GJ, Hozumi A. Recent progress and future directions of multifunctional (super) wetting smooth/structured surfaces and coatings. Adv Funct Mater. 2020;30:1907772.
43. Cassie ABD, Baxter S. Wettability of porous surfaces. Trans Faraday Soc. 1944;40:546–51.
44. Ma W, Ameduri B, Takahara A. Molecular aggregation structure and surface properties of biomimetic catechol-bearing poly[2-(perfluorooctyl)ethyl acrylate] and its application to super-amphiphobic coatings. ACS Omega. 2020;5:8169–80.
45. Fu C, Zhu HE, Mitsuishi M. Surface wettability of poly(vinylidene fluoride) nanoparticle assembly surfaces. Polym J. 2022;54:741–6.
46. Xiao YT, Yang WC, Zhou L, Hao HX, Bao Y, Yin QX, et al. Growth mechanism of the spherulitic propylthiouracil-kaempferol cocrystal: new perspectives into surface nucleation. CrystEngComm. 2021;23:2367–75.
47. Yang J, Cui YD, Chen MY, Wang Y, Xu SJ, Wu SG, et al. Transformation between two types of spherulitic growth: tuning the morphology of spherulitic nitroguanidine in a gelatin solution. Ind Eng Chem. 2020;59:21167–76.
48. Bünzli JCG. Benefiting from the unique properties of lanthanide ions. Acc Chem Res. 2006;39:53–61.
49. Yamamoto M, Ando K, Inoue M, Kanoh H, Yamagami M, Wakiya T, et al. Poly-β-ketoester particles as a versatile scaffold for lanthanide-doped colorless magnetic materials. ACS Appl Polym Mater. 2020;2:2170–8.